ACS APPLIED ENERGY MATERIALS

www.acsaem.org Article

Photonically Cured Solution-Processed SnO_2 Thin Films for High-Efficiency and Stable Perovskite Solar Cells and Minimodules

Nisha Sarda, Arya Vidhan, Susmita Basak, Preetam Hazra, Tejmani Behera, Sudeshna Ghosh, Ram Janay Choudhary, Arindam Chowdhury, and Shaibal K. Sarkar*

Cite This: https://doi.org/10.1021/acsaem.3c00232 Read Online

ACCESS | Metrics & More | Article Recommendations | Supporting Information

ABSTRACT: High-throughput fabrication of metal oxide thin films is always a bottleneck for solution-processed perovskite solar cells. Here, we report a rapid photonic curing process, with a well-controlled train of short light pulses, to develop bilayer (colloidal and blocking layer) SnO_2 thin films used as electron transport layers in perovskite ($(FA_{0.83}MA_{0.17})_{0.95}Cs_{0.05}PbI_{2.5}Br_{0.5}$, 1.62 eV band gap) photovoltaic devices (n−i−p architecture) with an optimized efficiency of 21.1% alongside good ambient and operational (MPPT) stability. The strong dependency of the photonic curing pulse parameters on device properties is investigated, and we established a corroboration between the chemical properties of the as-cured SnO_2 and the optoelectronic performance of the devices and the interface quality. Furthermore, we show that the futile removal of the chloride species in photonically cured SnO_2 is an added advantage against the thermally annealed ones regarding charge transport and lower interfacial recombination. Furthermore, the process is impeccably scaled up to demonstrate a series-connected minimodule (16 cm^2) with 18.2% efficiency.

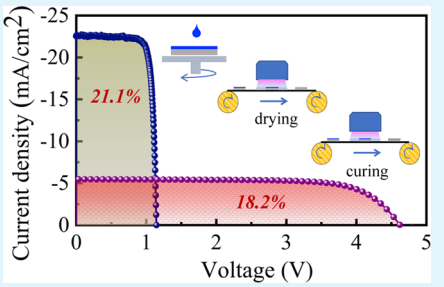

KEYWORDS: *photonic curing, high throughput, SnO_2, perovskite solar cells, minimodule*

INTRODUCTION

During the last decade, the meteoric rise of the photoconversion efficiency of hybrid halide perovskite-based solar cells suppressed many contemporary energy-harvesting devices by some margin.[1,2] From a promising 3.8% efficiency,[3] it has reached a value of 25.8% efficiency[4] within a reasonably short span of time. The overall improvement is often credited to a well-orchestrated evolution of materials and methods.[5,6] Bearing in mind recent developments in device stability,[7,8] the solution-processable perovskite technology is now set to be explored to comprehend the viability of low-cost photovoltaics. However, the feasibility of the lowered manufacturing cost can only be realized if the production throughput is optimized for the process, which is otherwise relatively unsophisticated, be it sheet-to-sheet (s2s) or roll-to-roll (r2r).[9] The advantages of the r2r over the s2s are twofold: higher throughput and choice of the plastic substrate, but with a caveat as the polymeric substrates are highly temperature-sensitive. Although the low-temperature processes for hybrid perovskite materials can possibly be well realized by now,[10−12] in a similar context, deposition of metal oxides is far more technologically challenging[13] due to the high formation energy. Considering the mechanical flexibility and the chemical nature of the substrates, the r2r process essentially demands the elimination of the rate-limiting equilibrium thermal annealing step from device fabrication. Use of solution-processed organic thin films as charge selective materials,[14,15] where thermal treatment is undesirable, or employing thermally stable flexible substrates like metal (foil or fiber)[16,17] or flexible glass,[18] can well suffice the technical need but is never a commercially viable option, in terms of both stability and cost, respectively. This opens up reconfiguring the possibilities where a low-temperature, high-throughput solution process needs to be developed without any compromise in the material quality, which can directly affect the device's performance.

In the majority of the reported literature where low-temperature processes are demonstrated, the processing time is either alarmingly high or reproducibility over a larger area is debatable. Assembled nanoparticle films, where the aqueous dispersion is coated and subsequently dried, are explored as carrier selective layers,[19,20] but often suffer from pinholes and lower shunt resistance. For the conventional thin film, often called a compact layer, novel low-temperature deposition techniques are also used, like laser annealing[21] (limited by surface area), UV,[22] or plasma[23] treatment. Also, incorporating the combustion chemistry in plasma-induced processes reduces the oxide formation time, but the device compatibility is yet unclear.[24] In recent times, rapid thermal annealing (RTA) has also been reported for metal oxide layer formation,[25] which

Received: January 26, 2023
Accepted: March 20, 2023

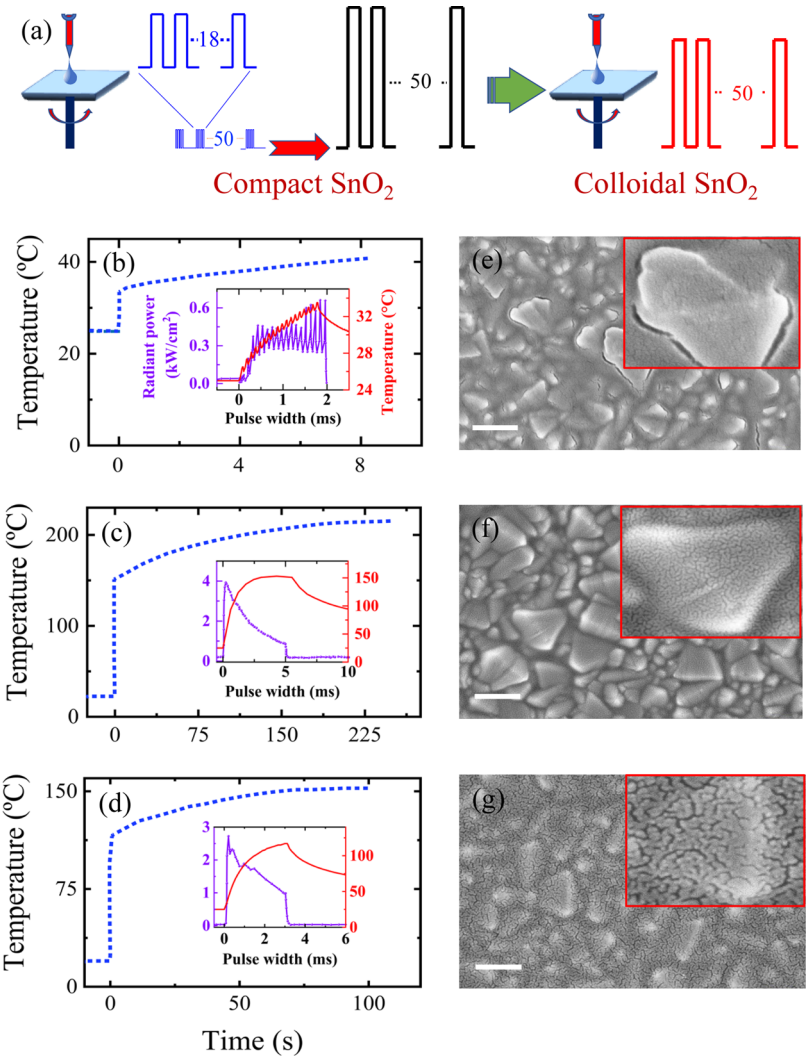

Figure 1. (a) Process flow diagram of compact and colloidal SnO_2 thin-film deposition and their subsequent photonic curing steps; the peak temperature profile of each photonic curing step for 50 consecutive pulses incident during the (b) drying step of the compact SnO_2 thin film, (c) curing step of the compact SnO_2 thin film, (d) curing step of the colloidal SnO_2 thin film (inset shows the profile of radiant power (purple) of every incident pulse and temperature profile (red) of the first incident pulse for corresponding steps). (e–g) Top-view SEM images of the SnO_2 thin films after drying, curing of compact SnO_2, and curing of colloidal SnO_2 deposited over FTO, respectively (inset shows the zoomed-in image of one FTO grain; scale bar = 200 nm).

significantly reduces the device processing time, but, due to the nature of the thermal cycling process, the applicability is, therefore, substrate-limited. In a similar route, photonically cured[26,27] (i.e., pulsed Xe) and also near-infrared-induced (either continuous or time-modulated) heating has also been demonstrated[28,29] to develop the perovskite layer only, which is, however, the least of concern due to its low formation energy. Nevertheless, the above-mentioned processes drive to a newer scientific domain where the feasibility of the nonthermal (conductive or convective) route for (be it photochemical or photon-induced thermochemical) wet film to crystalline metal oxide thin-film conversion is exhibited.

In recent times, the use of pulsed Xe light opens a newer paradigm[30] of perovskite device fabrication.[31] The short (μs–ms time) pulse of light with high peak power ($kW{\cdot}cm^{-2}$) and overall radiant energy (tens of $J{\cdot}cm^{-2}$) enables chemical changes of the wet film (often spin- or slot-die-casted), leading to the formation of thin solid films (oxides or perovskites). The true advantage of this technique lies in the form of significantly small light pulse duration alongside the differential thermal mass distribution between the wet film and the substrate, which inclusively results in insignificant thermal damage to the substrate. This process can be performed either in ambient or inside a glovebox and is, literally, independent of the substrate size, making it suitable for scaling up, either r2r or s2s. Although the process is technologically challenging in comparison to the conventional equilibrium heating process, it has a far-fetched economical advantage, as reported by Martin et al. from the techno-economic perspective.[9] In the context of perovskite solar cells, the challenge is twofold: (a) ambient processing of device-compatible perovskite materials where solution chemistry plays a vital role, but technologically it is less challenging due to the lower formation energy and higher absorptivity of the precursor solution; and (b) deposition of the metal oxide thin films where the formation energy is significantly higher. However, a common yet understated factor in both of these materials' development is the control over defect density, which plays a significant role in terms of both obtaining a higher efficiency and better operational stability.

https://doi.org/10.1021/acsaem.3c00232
ACS Appl. Energy Mater. XXXX, XXX, XXX–XXX

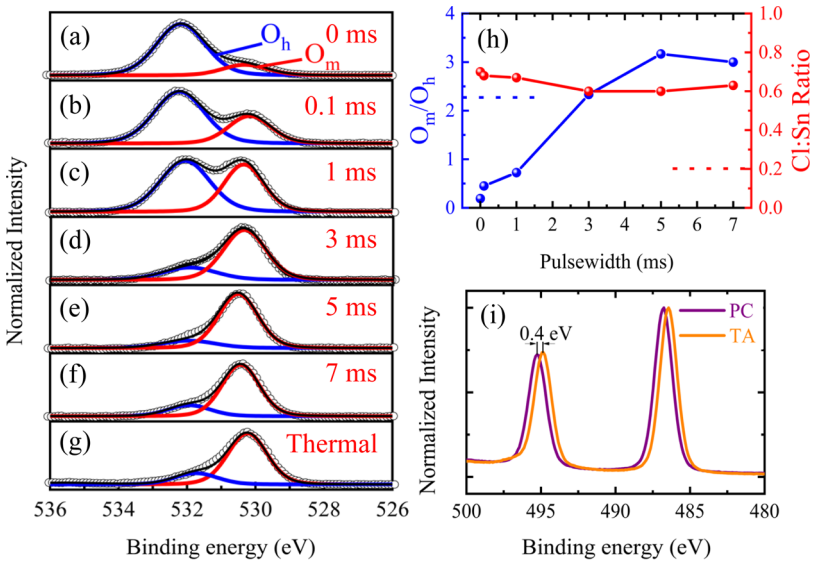

Figure 2. X-ray photoemission spectroscopy spectra. (a–g) Oxygen O 1s peak for varied pulse widths of the photonic curing process from 0 to 7 ms (capacitor voltage is kept at 450 V) and thermal SnO_2 thin film. Deconvolution of the O 1s peaks illustrated in two different aspects of oxygen bonding at 530.4 eV (red line, oxygen atoms in the M−O−M lattice) and 532.2 eV (blue line, oxygen atoms in the M−O−H). (h) Ratio of M-O−M(O_m) to M−O−H(O_h) (in blue) and the normalized chlorine content w.r.t tin (in red); dashed lines represent the thermally annealed SnO_2 film. (i) Sn 3d spectra of 5 ms and thermally annealed SnO_2.

Considering the band alignment with the widely used multication perovskite material, tin oxide (SnO_2) is always a well-targeted material to be developed by photonic curing. However, some significant efforts are also directed at developing the TiO_2 compact layer[32] and the mesoporous architecture[33] on both rigid glass and flexible polymer-based substrates. In continuation to a similar node, SnO_2 thin films in the form of conventional blocking layers[34] or assembled nanoparticulate films[35] were also developed by photonic curing. Both water[34] and ethanol[36] are used as solvents and photonically cured with a long pulse to form SnO_2 through the dehydroxylation mechanism. These results, though, paved the way and proved the viability of the technology applicable in perovskite devices; however, they apparently have given an impression of a low-performing device in comparison to the ones that are conventionally made with thermally grown SnO_2 (or TiO_2). In addition, there is a significant void in obtaining a detailed evaluation of the materials formation chemistry that can be directly corroborated with device performance.

In this work, we report the development of a bilayer SnO_2 (compact, followed by a colloidal layer, essential for the device) electron transport layer (ETL) through photonic curing on FTO-coated glass substrates for high-efficiency multication perovskite devices and also demonstrate the scalability with series-connected minimodules. From the material chemistry viewpoint, the focus was on substantiating the parametric analysis, during the materials development process, with the device's photovoltaic properties, and for a fair comparison, the findings are compared with the optimized thermally grown SnO_2. Our results unequivocally demonstrate that significant control over the photon pulse, in terms of both the time sequence and energy delivery, is obligatory to obtain the needed quality of oxide material, not only for high photovoltaic efficiency but also to establish control over the defect density, which otherwise can be detrimental for long-term operational stability.

RESULTS AND DISCUSSION

As a standard protocol in SnO_2-based perovskite photovoltaic devices, the ETL comprises a bilayer of tin oxide, which is individually spin-coated and subsequently photonically cured. For the blocking layer, a well-stirred solution of 0.05 M tin(IV) tetrachloride pentahydrate ($SnCl_4 \cdot 5H_2O$) in isopropanol alcohol (IPA) is used, whereas a diluted aqueous dispersion of colloidal SnO_2 (~3.8 wt %) is used for the thin overlayer. It is worth mentioning that for the succeeding layer deposition, only if the wait time between two consecutive castings is high, O_3 treatment is found helpful solely for better wetting purposes. Detail of the processes is explained in the Experimental section, while the overall pulse sequences are depicted in Figure 1a. Notably, here, the whole process is segmented into three: drying (blue) of the wet film, followed by curing (black) to form the oxide and, finally, the annealing of the colloidal layer (red). Therefore, from the process, apparent from Figure 1a, it is well understood that there is no conventional thermal treatment at any stage, which made this process unique and, thus, high throughput is obtained. Figure 1b–d depicts an indicative evolution of the simulated peak temperature of every consecutive pulse during the course of the curing process, while the inset represents the radiant power of a representative pulse (in purple) and the change in the temperature profile of the material during the first incident light pulse (in red). Understandably, the radiant power is invariant during consecutive pulses, while the temperature profile evolves during the overall process. The resultant surface morphology after every process step is shown in Figure 1e–g.

In the drying step, the motivation is to remove the solvents through mild heating, which is optimized by a series of 50 pulses of light, giving rise to a total radiant energy density of 0.3 $J \cdot cm^{-2}$ on the sample surface. Unlike a train of single pulses, here, the choice of dividing every single pulse into a number of micropulses is to limit the obtained temperature and thereby limit the drying stage from the material formation stage. As per the simulation, the said process raises the

https://doi.org/10.1021/acsaem.3c00232
ACS Appl. Energy Mater. XXXX, XXX, XXX−XXX

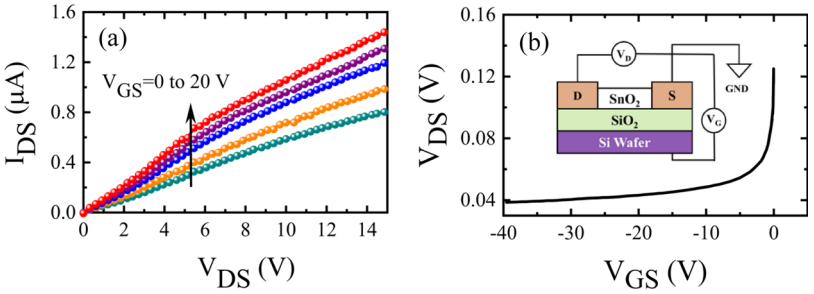

Figure 3. (a) Output characteristics for the photonically cured 5 ms pulse width SnO_2-TFT with V_{GS} varied from 0 to 20 V. (b) Transfer characteristics for the photonically cured 5 ms pulse width SnO_2-TFT at V_{DS} = 15 V. The inset shows the schematic of the TFT device structure with 30 μm channel width.

temperature of the sample surface to ca. 35−40 °C for 8 s, as shown in Figure 1b. To optimize the curing process, the dried thin films were subjected to a train of optimized 50 light pulses, each having energy densities of 2.1 J·cm^{-2} (250 V), 5.1 J·cm^{-2} (350 V), and 9.7 J·cm^{-2} (450 V, instrumental limiting parameter) while keeping the simulated temperature profile (Figure S1) as a reference parameter. Considering previously optimized thermally grown SnO_2 processes, where the annealing temperature was optimized to 180 °C and corroborating the device parameters obtained (Figure S2), we kept the applied voltage to 450 V for further investigations. Furthermore, as a final stage of optimization, the lamp voltage was kept to the above-optimized value (450 V) and the pulse width was varied (from 0, essentially dried, to 7 ms) while keeping the total number of pulses to 50 (see the Experimental section and Tables S1 and S2). Since the process of energizing the Xe lamp is through a capacitive discharge process, it is expected that increasing the pulse width (i.e., discharging time) will result in a nonlinear rise in the peak power but to a limit that is decided by the applied voltage. It is worth mentioning here that with increasing the pulse width, the nature of the radiant power is not a constant (hence the temperature) over time; rather, it reaches the peak power sharply and is followed by a nonlinear decay as shown in Figure S3. Thus, increasing the width of the pulse essentially results in two important things: (a) sustaining the peak temperature for a longer time and (b) stretching the temperature decay characteristics and resulting in an indirect control over the sample cooling that affects the overall crystallization. The variation of the pulse width, at constant applied voltage, therefore, provides finer control over the formation of the material and is studied with X-ray photoelectron spectroscopy (XPS) as discussed below.

Elemental compositions and chemical states of the as-formed photonically cured SnO_2 are investigated through XPS as a function of the curing pulse width only while keeping the rest of the parameters unaltered. Figure 2a−g shows the high-energy-resolution X-ray photoelectron spectra of the O 1s spectra, which are resolved into two types of components relating to the chemical nature of the oxygen bonding. Please note that the corresponding survey scans are shown in the Supporting Information (SI) (Figure S4a−g). The peak around the energy 530.3 ± 0.1 eV corresponds to the tin oxygen binding energy, which is in the metal oxide lattice (M−O−M) correlation, while the peak at 532.1 ± 0.1 eV shows hydroxyl oxygen binding energy (M−O−H). Our study systematically reveals the relative evolution of the M−O−M peak against M−O−H by increasing the pulse width while keeping the other process parameters the same (Figure 2h), indicating the formation of the SnO_2 material. Notably, little changes in the relative ratio are found when the pulse width is increased from 5 ms (∼3.16) to 7 ms (∼3), which is indicative that the curing process probably reached a saturation limit with 5 ms pulse width. For a fair comparison, the O 1s peak of the thermally grown SnO_2 film is also depicted in Figure 2g. The distinctive difference, though marginal but reproducible, between the thermally annealed and photonically cured and SnO_2 films is the relatively higher presence of metal hydroxide with respect to the ones that are cured with 5 or 7 ms pulse width. This certainly indicates the poorer conversion of the precursor to the metal oxide by thermal annealing, even though it is optimized for the devices. However, the striking difference between the photonically cured and thermally annealed SnO_2 is the relative presence of the chloride species (refer to Figures 2h and S5). The chlorine-to-tin ratio in PC-SnO_2 is ca. 0.6, while for TA-SnO_2, it is at or around 0.2. A stronger presence of chloride species in PC-SnO_2 can also be seen in the absolute peak position of the Sn $3d_{5/2}$ and $3d_{3/2}$ binding energies, which is ∼0.4 eV higher for PC-SnO_2 with respect to TA-SnO_2, as shown in Figure 2i. It is important to mention that the presence of chlorine is, however, not limited to the surface but is also present in the crystal lattice. It is therefore expected that while the surface chloride species can help in the nucleation and the growth process of the perovskite absorber layer and provide better interfacial quality, the bulk chloride species is responsible for the nonstoichiometric defects in SnO_2, which can be influential in improving the charge transport properties.[37]

To investigate the relative differences in the electronic properties, thin-film transistors (TFTs, bottom gate assembly) on p-type Si/SiO_2 substrates (thermally grown 285 nm of SiO_2) with a channel length of 30 μm are made with 5 ms, 7 ms, and thermal SnO_2 thin films. A detailed description of the fabrication process is given in the SI. To clarify the standpoint, here, the aim was not to make an optimized TFT but rather to understand the differences of its electronic characteristics of the channel material, deposited by the above-mentioned processes. The 5 ms SnO_2 films show reasonable TFT characteristics (equivalent characteristics are obtained for 7 ms SnO_2 films as well, and shown in Figure S6a,b) as shown in Figure 3a, where the drain-to-source current (I_{DS}) is plotted as a function of the drain-to-source voltage (V_{DS}) with varied gate-to-source voltages (V_{GS}). Corresponding gate leakage currents (∼nA) with varied V_{DS} are shown in Figure S6c,d. Notably, the said device is an n-MOS architecture, which is in the normally ON state and, expectedly, the negative gate bias is applied to move the characteristics toward the OFF state. The

https://doi.org/10.1021/acsaem.3c00232
ACS Appl. Energy Mater. XXXX, XXX, XXX−XXX

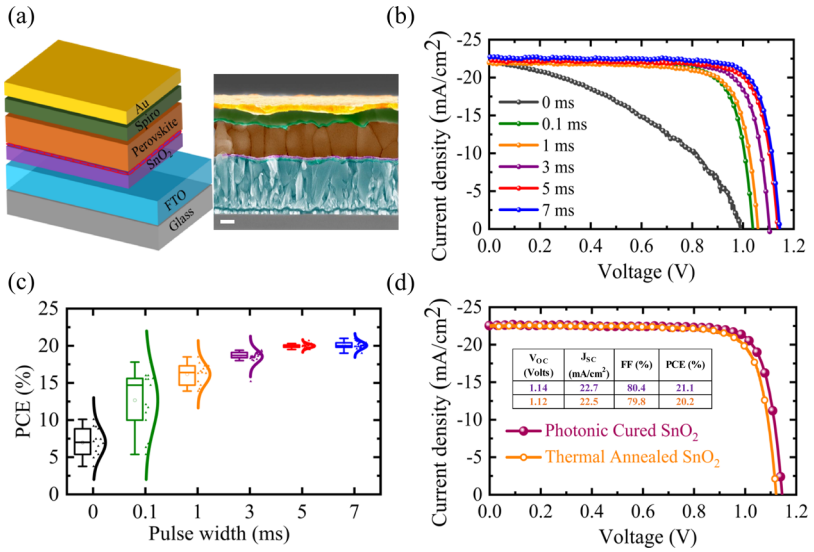

Figure 4. (a) Schematic diagram with cross-sectional SEM image of the perovskite solar cell device with a photonically cured compact and colloidal SnO_2 thin film deposited as ETL (scale bar = 200 nm). (b) Champion light $J-V$ characteristics in the reverse scan obtained by employing a photonically cured compact SnO_2 layer with varied pulse widths from 0 to 7 ms. (c) Box plot of PCE using a photonically cured compact SnO_2 layer with varied pulse widths from 0 to 7 ms. (d) Light $J-V$ characteristics of perovskite solar cells at 100 mW·cm^{-2} (1 sun) intensity employing a photonically cured (purple solid dots) and thermally annealed (orange hollow dots) compact and colloidal SnO_2 thin film deposited as ETL delivering PCEs of 21.1 and 20.2%, respectively.

previous statement can be corroborated with the transfer characteristics (Figure 3b) of the same device. Here, the drain current (I_d) is measured with a varied gate voltage (V_G) under a fix drain-to-source bias, 15 V here. The characteristics convincingly indicate that the device predominantly stays in the linear regime and even a reasonably high enough gate voltage has been proven to be insufficient to switch it to the saturation stage. Hence, the linear current equation and its subsequent derivable are assumed (see the SI for the detailed calculation) to estimate the carrier concentration, which is found to be ca. $1.8 \pm 1.6 \times 10^{18}$ cm^{-3}, while the estimated mobility is $\sim 6.3 \times 10^{-3}$ cm^2/V.s. In comparison to the above, the as-deposited thermally grown one shows no measurable TFT-like behavior. Here, the obtained signal is on the order of the leakage current, as shown in Figure S6e,f. While the morphological differences can play a significant role in the lateral transport over the channel length, which is essentially grain-boundary-limited,[38] the defect density can also be crucial here, considering the existence of a significantly higher amount of chloride species in PC-SnO_2 in comparison to TA-SnO_2. However, such an analysis is not essentially within the scope of this report, but certainly, we can hypothesize that the chloride species in PC-SnO_2 is certainly beneficial for the perovskite–SnO_2 interface either by passivation or by promoting better crystallization of the perovskite layer as reported in the literature.[39]

Considering the fact that the material and the process under investigation are aimed to be used in perovskite devices, a set of devices (multication perovskite $(FA_{0.83}MA_{0.17})_{0.95}Cs_{0.05}PbI_{2.5}Br_{0.5}$ as an absorber layer and spiro-OMeTAD as the hole transporting layer) employing SnO_2 as ETL is photonically cured with a varied pulse width (0–7 ms). The device architecture and the cross-sectional SEM image are shown in Figure 4a (SEM images of the perovskite layer with the representative SnO_2 layer are given in Figure S7). In addition to the thin film of SnO_2 (often referred to as the compact layer), an additional thin layer of colloidal SnO_2 was also spin-coated and subsequently cured by photonic pulses in the same line of process, as indicated in Figure 1a. Incorporating the colloidal SnO_2 layer (unfunctionalized) is important as it enhances the charge extraction and effectively removes the hysteresis in the $J-V$ characteristics. For the optimization of the colloidal layer annealing process, we kept the hysteresis index as the check parameter and the thermally annealed colloidal layer on the photonically cured compact SnO_2 layer as the control (refer to Figure S8). With an optimized colloidal SnO_2 layer, representative light $J-V$ characteristics of the devices made with a varied pulse width of the photonic curing process for the compact SnO_2 layer are shown in Figure 4b, and the calculated efficiency values with statistical distribution are shown in Figure 4c, while the individual device parameters (J_{SC}, V_{OC}, and FF) are shown in Figure S9. The champion device was obtained with 21.1% efficiency (Figure 4d), and for a fair comparison, device characteristic from the thermally grown SnO_2 is also shown in the same figure. From the figures (Figures 4b and S9a), it is clearly evident that there is not much change in the short-circuit current density (J_{SC}) on increasing the pulse width, but certainly, the median of the open-circuit potential (V_{OC}) values is shifted from ca. 0.75 V to ca. 1.1 V (Figure S9b). It is important to note that the distribution of the device parameters, majorly V_{OC} and fill factor (Figure S9b,c, respectively), also gets narrower monotonously until 5 ms and tends to saturate thereon. The improvement of the photovoltaic parameters with increasing the pulse width can largely be corroborated by the XPS results, which evidently suggest better oxide formation. This strongly indicates a systematic improvement in the oxide–perovskite interface quality with increasing the pulse width as it is very obvious that both the fill factor (FF) and the V_{OC} depend strongly on the nonradiative interfacial recombination.

To validate the aforementioned dependency of the device parameters with pulse width, we performed the electro-luminescence (EL) and photoluminescence (PL) measure-

https://doi.org/10.1021/acsaem.3c00232
ACS Appl. Energy Mater. XXXX, XXX, XXX–XXX

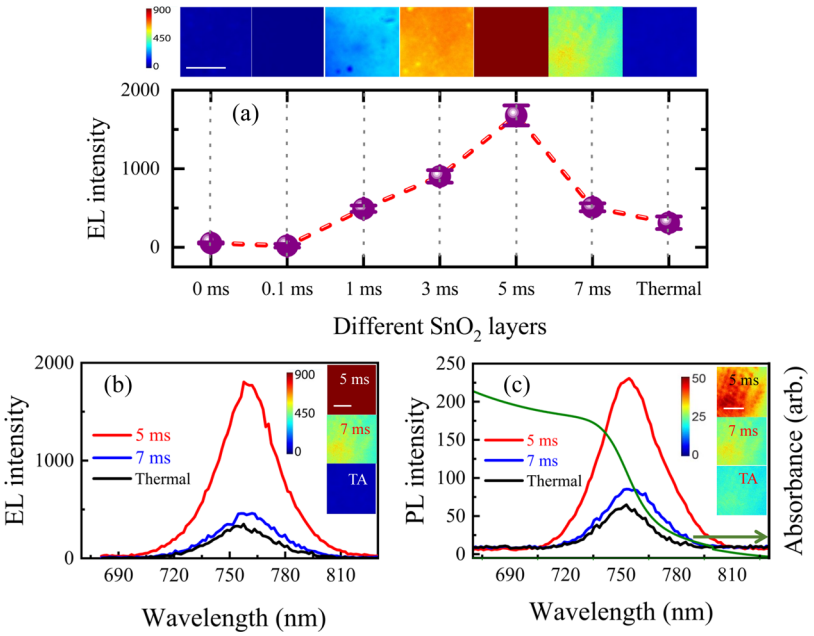

Figure 5. (a) Evolution of the EL intensity of the device employing varying pulse widths photonically cured and a thermal SnO_2 thin film deposited as ETL alongside their corresponding EL images. (b) EL spectra of devices using 5 and 7 ms and the thermal SnO_2 thin film deposited as ETL alongside their EL images. (c) PL spectra of devices of 5 and 7 ms and the thermal SnO_2 thin film deposited as ETL with their PL images using 532 nm DPSS laser. All EL and PL intensities are in counts per 500 ms, and the scale bar in all EL and PL images is 10 μm. Alongside, the optical absorbance is also plotted.

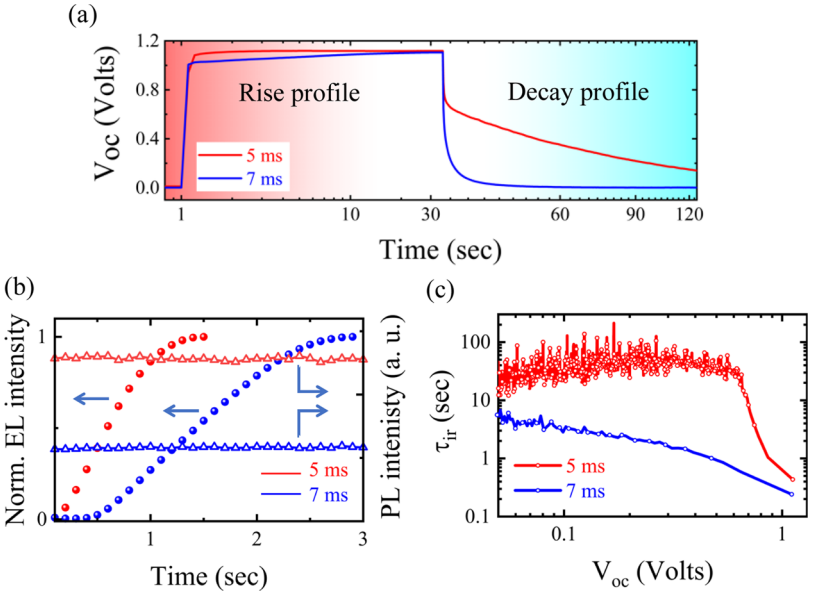

Figure 6. (a) Transient open-circuit potential (V_{OC}) rise and decay. (b) Normalized EL intensity (solid circle) and PL intensity (hollow triangle) evolution with time. (c) Instantaneous relaxation time profile of devices with 5 and 7 ms photonically cured SnO_2 thin films deposited as ETL, indicating the quality of the SnO_2−perovskite interface.

ments, both imaging and spectroscopy, under the steady state (representative time-resolved PL is shown in Figure S10), on representative samples in the custom-built setup (see the SI). Here, the devices are forward-biased at 1.5 V, and the dark current is similar to that of J_{SC}, indicating that the quasi-Fermi-level splitting under the applied bias is similar to that under the device operating condition. Figure 5a shows the EL intensity, both in the absolute count and in the corresponding images, as a function of the pulse width. For a fair comparison, EL characteristics of the device with thermally grown SnO_2 are also shown alongside. Expectedly, we find an improvement of the EL intensity with increasing the pulse width, an understanding extended from the discussion above (Figure 4c). However, surprisingly, a significant decrease in the EL intensity is found in the devices where the pulse width is increased from 5 to 7 ms (Figure 5b), which is rather unanticipated as the chemical composition of the SnO_2 layers involved in these devices is nearly identical unlike the 3 ms ones, which is more unambiguous as discussed earlier (Figure 2). Considering the fact that a higher EL quantum yield

https://doi.org/10.1021/acsaem.3c00232
ACS Appl. Energy Mater. XXXX, XXX, XXX−XXX

corresponds to the reduction of the nonradiative recombination losses in the device (essentially interface, here) that fundamentally drives the V_{OC} closer to its radiative limit but, from the light $J-V$ characteristics, no significant change in V_{OC} is found between these two subjective devices. It is somewhat taken as obvious that the enhancement in the EL intensity is an indication of the improved V_{OC} but with a logarithmic dependency.[40] Here, the difference in the EL intensity between the 5 and 7 ms is only 3-fold (Figure 5b), essentially reflecting that the expected theoretical difference in the V_{OC} is only in the range of a few millivolts,[41] which often remains unnoticed during the standard $J-V$ measurements due to the high scan rate and the resolution of data points. To substantiate our observation in the EL, we performed photoluminescence (PL) measurements on similar devices (5 and 7 ms) in the same experimental setup, and the spectra are shown in Figure 5c. For reference, a pristine perovskite film on a thin colloidal Al_2O_3-coated glass slide was used, as shown in Figure S11. Alongside, the device fabricated with thermally grown SnO_2 is also represented. Evidently enough, the PL intensity is significantly high in the 5 ms device in comparison to the others without any spectral shift. Considering the fact that the PL is thought to be predominantly coming from the bulk of the perovskite but is highly sensitive to the surface recombination velocity, our observation, therefore, predominantly echoed the ones that are observed from the EL measurements. Thus, the conjugated understanding from the EL and PL measurements indicates significantly lowered nonradiative recombination losses at the perovskite−SnO_2 interface when the oxide layer is deposited with 5 ms pulse width.

To establish the understanding drawn from the spectroscopic investigations, we performed time-dependent optoelectronic measurements, which were aimed at elucidating the effect of the interfacial properties on the transient response of the device. It is a well-established fact that the surface defects in the oxide material significantly influence the dynamics of the mobile ionic species in the perovskite material and hence the stability of the device.[8] Thus, it can be furthermore inferred that the redistribution of the accumulated ionic species influenced by the instantaneous change in the photoinduced internal electric field distribution is subjective to chemical interaction between the mobile ions and the oxide surface. We try to investigate the relative difference in the interface properties of the 5 and 7 ms devices by the momentaneous change in the V_{OC} (both rise and decay) influenced by the large perturbation of incident light (100 mW·cm^{-2}), as shown in Figure 6a. An illumination pulse length of 30 s is needed to obtain the stabilized V_{OC} as the devices were kept unperturbed both optically and electronically before the measurements. Both the 5 and 7 ms devices reach the same V_{OC} value as expected, with a slender but notable difference in the rise characteristics. The stabilized V_{OC} value was instantaneously reached by the 5 ms device, while for the 7 ms device, there was a steep upsurge followed by a slower rise before it reached the saturation value.

The V_{OC} represents the difference between the quasi-Fermi-level splitting (QFLS) and is represented by $V_{OC} \cong \frac{k_B T}{q} \ln\left(\frac{n^2}{n_0 p_0}\right)$, where k_B represents the Boltzmann constant, T is the absolute temperature, and q is the elementary charge. The n_0 and p_0 represent the intrinsic carrier concentration, and n is the carrier concentration. Thus, the rise in V_{OC} (Figure 6a) can be seen as an instantaneous relation between the carrier generation and recombination. The slower rise in the V_{OC} of the 7 ms device with respect to the 5 ms device hence can be well attributed to the slower buildup of the photogenerated charge carrier density. Noteworthy here, for both the 5 and 7 ms devices, the process of photoinduced redistribution of the internal electrostatic potential is not mediated by any variation of the nonradiative recombination pathways as the PL intensity of the respective devices remains time-independent, unlike the EL intensity, which gets enhanced, as shown in Figure 6b. Change in the EL intensity is expected with the time-dependent change in $V_{OC,}$ but here the time scale is significantly different; however, the relative differences between the 5 and 7 ms devices are persistent from both the time-dependent V_{OC} and EL intensity rise measurements. The time-dependent rise in EL intensities therefore represents the slow trap-filling and stabilization of the charge trap states in the SnO_2 itself, which is evidently higher in the 7 ms than in the 5 ms device. Furthermore, we postulate that the relatively slower changes in the ionic movement and hence change are the keys to the V_{OC} rising and not the alteration of the nonradiative recombination kinetics. Thus, a relatively faster rise in the V_{OC} in the 5 ms device with respect to the 7 ms one is essentially an indication of a better interface, which is furthermore discussed below with the open-circuit voltage decay (OCVD) measurements.

From the experimentally obtained OCVD characteristics (Figure 6a) of the 5 and 7 ms devices, two distinct decay patterns are noticed. The 5 ms device shows a remarkably slow decay process, while the 7 ms device reveals a rapid decay. The instantaneous relaxation time[42] $\tau_d(V) = \left(\frac{1}{V}\frac{dV}{dt}\right)^{-1}$ is also shown in Figure 6c. As seen from the figure, the relaxation time is not constant but varies throughout the decay process. During the initial stage, after switching off the light, the decay process is solely electronic and governed by the built-in potential. Thus, the observed t_d value is similar in both subjective devices. However, thereafter, the t_d value progressively deviates between these devices. It is understood[43] that the overall V_{OC} in the perovskite devices is an additive of the built-in potential (V_{bi}) and the electrostatic potential (V_{elect}). Notably, the decay process of V_{elect} is subjected to the redistribution of the mobile ionic species influenced by $V_{bi,}$ and the kinetic response is much slower; hence, a considerable voltage is measured over a much longer time range (a few minutes) after switching off the light, as we see for the 5 ms device (Figure 6b). Any chemical interaction between the accumulated ions (either under forward bias or under sustained V_{OC} conditions) and the interfacial defects intimidate the kinetic response of the mobile ions. Upon removal of the light, the large concentration of carriers at the oxide−perovskite interface results in rapid recombination, resulting in a faster drop in the V_{OC}, which is what we can see for the 7 ms devices (Figure 6b). Our observation is in accord with the one reported by Gottesman et al., where a thin interfacial layer of PCBM between the TiO_2 and perovskite absorber layer significantly changes the interfacial defect dynamics.[44] Thus, the OCVD analysis reiterates the inference drawn from the EL and PL measurements, shown previously, and conclusively demonstrates that slender *overannealing* (the 7 ms sample with respect to the 5 ms one) results in a significant change in the interfacial defects, which is also seen in the thermally annealed samples as well but not so drastically.

To understand the device stability, shelf-stability and under continuous operation with maximum power-point tracking

https://doi.org/10.1021/acsaem.3c00232
ACS Appl. Energy Mater. XXXX, XXX, XXX−XXX

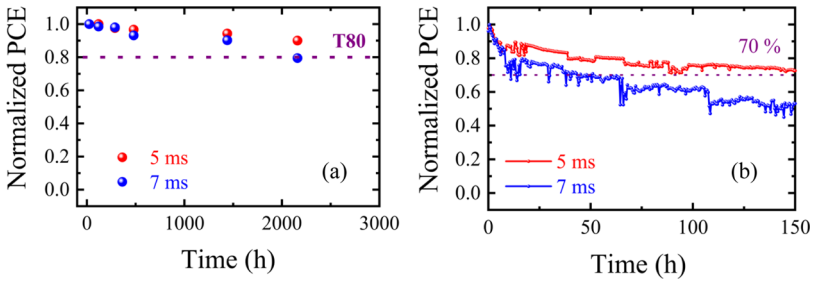

Figure 7. (a) Intermittent PCE obtained from the light $J-V$ scan of unencapsulated devices with 5 and 7 ms photonically cured SnO_2 ETL measured over a span of 2160 h; devices were stored in ambient dark conditions. (b) Maximum power-point (MPP) tracking of devices with 5 and 7 ms photonically cured SnO_2 ETL with active loads illuminated with 1 sun equivalent intensity.

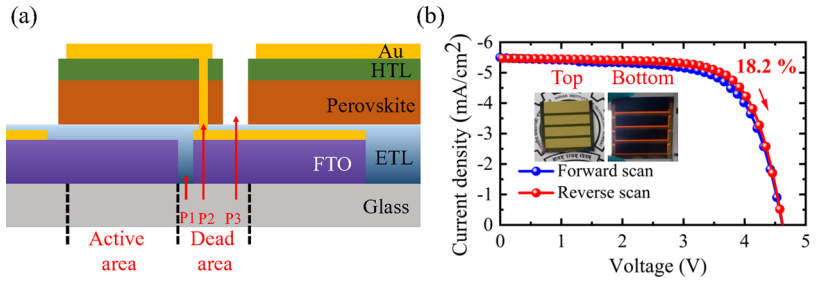

Figure 8. (a) Schematic illustration of series-connected minimodules employing the P1–P2–P3 scribing strategy with the photonically cured SnO_2 thin film as ETL on an area of 16 cm^2 and an active area of 6.8 cm^2. (b) Light $J-V$ characteristics of perovskite solar minimodules at 100 $mW{\cdot}cm^{-2}$ (1 sun) intensity employing a photonically cured thin film deposited as ETL in both forward (blue) and backward (red) scan directions delivering PCEs of 17.2 and 18.2%, respectively. The inset shows the top and bottom views of the minimodule with the photonically cured ETL.

(MPPT) were performed, and a set of representative data is shown in Figure 7a,b, respectively. For the shelf-stability, devices were measured intermittently while kept unattended over a period of 3 months under an ambient atmosphere with an average humidity of ~60%. The resultant efficiency values of these subjective devices measured over time are shown in Figure 7a. The figure clearly depicts that the 7 ms device reached 80% of its initial efficiency after 2160 h (~3 months), while within the same time frame, the 5 ms device retained 90% of its initial efficiency. A similar set of devices was also kept under MPPT, as shown in Figure 7b. Under continuous illumination and MPPT measurements over 150 h of operation, the 5 ms device reduced by 30% from its original efficiency, whereas the 7 ms device reached 53% of its initial efficiency value. Thus, in an unambiguous way, it is clear that the 5 ms devices show better stability than the 7 ms devices, which is essentially corroborated by the better interfacial characteristics, and it is a well-studied phenomenon in perovskite devices.[45]

Finally, the optimized photonic curing parameters are exercised to obtain larger area devices as a natural extension due to the optical uniformity over a wider region. This enables one to overcome the nonuniformity arising in the resistive heaters. Here, we choose to elucidate a minimodule with a total area of 16 cm^2, while the effective active area is 6.8 cm^2, which is subdivided into four series-connected subcells of equal dimensions. The architecture and the scribes are indicated in Figure 8a, while the details of the process are explained in the Experimental section. Representative device characteristics are shown in Figure 8b depicting an efficiency of 18.2%. Notably, the V_{OC} of the minimodule is 4.63 V, indicating that the individual cell voltage of ca. 1.15 V is slightly higher than the small-area devices, as shown above. It is to be considered that while the minimodule is measured with the full area illumination, for better reproducibility, the small-area devices are measured with the shadow mask. Thus, the uncompensated contribution of the dark current often limits the overall achieved V_{OC} in the smaller-area devices. Although the minimodules represented here are far from optimized, the intention here is not to elaborate on the overall efficiency value but to elucidate that the process we report is seamlessly scalable to a larger area.

CONCLUSIONS

In conclusion, we report the development of the critical process parameters for the bilayer SnO_2 ETL by the photonic curing process with strong feedback from corroborating materials chemistry and device characteristics. Although the applied voltage to the light source is indeed the primary factor that drives the material's formation chemistry, it is not necessarily the sole parameter for optimal device performance. We have shown an optimized process by varying the pulse width, number of pulses, and the nature of flash sequence required for the optimized performing devices. Although it is obvious that an underprocessed material will result in suboptimal device performance, here, we emphasized the fact that a slender overoptimized process can generate substantial surface defects as studied by EL, PL, and OCVD measurements. Here, we report that a SnO_2 ETL, cured with a series of 50 pulses of 5 ms pulse width, recorded 21.1% efficiency in a small-area (0.12 cm^2) perovskite device. We interpret better stability of the 5 ms devices against the 7 ms devices in terms of superior interface quality. Because of the uniformity in the illumination zone, the process is seamlessly scaled up to form a series-connected minimodule of area 16 cm^2 with an efficiency of 18.2%. Through this report, we have demonstrated an on-the-fly process to deposit SnO_2 ETL, which can be further tuned for the roll-to-roll processes.

https://doi.org/10.1021/acsaem.3c00232
ACS Appl. Energy Mater. XXXX, XXX, XXX−XXX

EXPERIMENTAL SECTION

Photonically Cured SnO_2 ETL Fabrication. The precursor solution was a well-stirred 0.05 M $SnCl_4.5H_2O$ (Sigma-Aldrich) in anhydrous IPA. The deposition is a two-step process: spin-coating on UV-ozone-treated FTO substrates at 2000 rpm for 45 s followed by photonic curing (NovaCentrix PulseForge Invent equipped with one 500 V lamp driver and 1.5 kW power). The photonic curing is done in two continuous but subsequent two-step processes: drying and curing. For the drying step, low-voltage pulses were applied (optimized with 50 pulses, where each pulse is subdivided into 18 smaller pulses, each with 75 μs on time and separated by 25 μs) in order to remove the traces of IPA followed by high-voltage pulses to crystallize the material (capacitor voltage: 450 V). An additional colloidal layer of SnO_2 was deposited by spin-coating and subsequent photonic curing. A SnO_2 colloidal dispersion solution diluted using deionized water in a 1:3 v/v ratio was used for the same. The detailed parameters of photonic curing (PC) conditions and energy densities used in every step are given in Tables S1 and S2, respectively.

Thin-Film Characterization. The TFT devices were characterized by an *in-house* setup employing a probe station connected to two separate Keithley 2450 source meters (each for drain and gate terminals). The detailed process is explained in the Supporting Information. X-ray photon spectroscopy (XPS) measurements were carried out using the Omicron energy analyzer (EA-125) with an Al k-α (1486.6 eV) X-ray source. Field emission scanning electron microscope (FESEM) images were obtained using a Carl-Zeiss Ultra 55 system.

Simulation. The surface temperature profiles w.r.t. temperature were simulated using NovaCentrix SimPulse software considering all of the process parameters and the percent light absorbed by the material. This software only processes the heat transfer process and light absorption by the sample; any photochemical processes were neglected during simulations.[30] The glass/FTO/SnO_2-precursor sample stack was modeled as 2200 μm soda-lime glass and 680 nm FTO. The simulations were performed in the surface absorption mode with 16% absorption. This value was determined from the bolometer absorption measurement by measuring the radiant energy absorbed by a calibrated bolometer at PC. The surface absorption of the glass/FTO/SnO_2-precursor sample was measured by the difference in radiant energy absorbed by the bolometer with and without the sample while taking the substrate reflection into account. This method estimates that the surface absorption for the glass/FTO/SnO_2-precursor is 16% with a standard deviation of 0.2%.

Solar Cell and Minimodule Fabrication. Triple cation solar cells were fabricated with the precursor $(FA_{0.83}MA_{0.17})_{0.95}Cs_{0.05}PbI_{2.5}Br_{0.5}$ dissolved in DMF/DMSO (4:1 volume ratio). The spiro-OMeTAD was used as the hole transport and gold was deposited as the top contact. The whole process of fabrication of bilayer thermal SnO_2 ETL and the device has been explained somewhere else.[8] For minimodule fabrication, patterned FTO substrates of size 4 cm × 4 cm (Xinyan technology Ltd.) were used employing a photonically cured compact SnO_2 layer. All of the steps were kept the same as described in the cell fabrication unless otherwise mentioned. A thin strip of gold of thickness 60 nm was deposited on FTO substrates near the electron collection side of each subcell. After depositing the gold layer, the compact layer was deposited by photonic curing. After depositing the compact layer, the colloidal dispersion layer of SnO_2 and the mesoporous Al_2O_3 nanoparticle layer was spin-coated sequentially before perovskite film fabrication. Both films were annealed at 150 °C for 30 min. The Al_2O_3 nanoparticle dispersion in IPA was diluted by a volume ratio of 1:6 and spin-coated at 6000 rpm for 45 s. After that, a perovskite absorber, spiro, and gold metal contact were deposited to connect four cells connected in series.

Device Characterization. The $J-V$ measurements were performed by a Class A xenon lamp from Abet Technologies with the light intensity calibrated at 100 mW·cm^{-2} with the help of a Newport silicon reference cell. A light aperture of 3.14 mm^2 was used for the measurements, and a biologic potentiostat SP-150 was used as the source meter. Open-circuit voltage decay (OCVD) was measured in the Wavelabs Sinus 70 solar simulator with a self-calibrating setup. EL and PL microspectroscopy measurements were performed with a home-built wide-field inverted epifluorescence microscope (Nikon Eclipse Ti2). The detailed process is explained in the Supporting Information.

Stability Measurement. Intermittent $J-V$ measurements were performed by a Class A xenon lamp from Abet Technologies with the light intensity calibrated at 100 mW·cm^{-2}. The intermittent measurements were done on the devices stored in ambient conditions without any encapsulation. Maximum power-point tracking was performed with the help of a Wavelabs Sinus 70 solar simulator with a self-calibrating setup. The devices were encapsulated with atomic layer deposition of Al_2O_3 thin films before the MPP tracking. The MPP data acquisition was done on a 16-channel SMU from Infinity PV with Infinity PV software where six channels were simultaneously kept running along with active loads connected to all of the channels individually.

ASSOCIATED CONTENT

Supporting Information

The Supporting Information is available free of charge at https://pubs.acs.org/doi/10.1021/acsaem.3c00232.

Summary of photonic curing conditions of bilayer SnO_2 thin-film fabrication, summary of energy density provided in each photonic curing step, peak simulated temperature profile of the SnO_2 thin film at different capacitor voltages, $J-V$ characteristics of devices at different capacitor voltages, experimental radiant power and simulated temperature profile of the SnO_2 thin film at different pulse widths, wide-spectrum XPS spectra of the SnO_2 thin film at different pulse widths, XPS spectra of Cl 2p of SnO_2 thin films, transfer characteristics and gate leakage current profile of the SnO_2 TFT device in different conditions, SEM of triple cation perovskite films coated on the photonically cured and thermally annealed SnO_2 thin film, statistical distribution of the hysteresis index of devices for the photonically cured colloidal SnO_2 thin film, statistical distribution of device parameters of devices with different pulse widths, TRPL of the perovskite film on photonically cured and thermally annealed SnO_2 films; and PL spectra of triple cation perovskite thin films (PDF)

AUTHOR INFORMATION

Corresponding Author

Shaibal K. Sarkar − *Department of Energy Science and Engineering, Indian Institute of Technology Bombay, 400076 Mumbai, India;* orcid.org/0000-0001-6788-9738; Email: shaibal.sarkar@iitb.ac.in

Authors

Nisha Sarda − *Department of Energy Science and Engineering, Indian Institute of Technology Bombay, 400076 Mumbai, India*

Arya Vidhan − *Department of Energy Science and Engineering, Indian Institute of Technology Bombay, 400076 Mumbai, India*

Susmita Basak − *Department of Energy Science and Engineering, Indian Institute of Technology Bombay, 400076 Mumbai, India*

Preetam Hazra − *Department of Energy Science and Engineering, Indian Institute of Technology Bombay, 400076 Mumbai, India*

https://doi.org/10.1021/acsaem.3c00232
ACS Appl. Energy Mater. XXXX, XXX, XXX−XXX

Tejmani Behera − *Department of Chemistry, Indian Institute of Technology Bombay, 400076 Mumbai, India;* orcid.org/0000-0003-2995-9293

Sudeshna Ghosh − *Center for Research in Nanotechnology and Nanoscience, Indian Institute of Technology Bombay, 400076 Mumbai, India*

Ram Janay Choudhary − *UGC − DAE Consortium for Scientific Research, Indore 452013, India;* orcid.org/0000-0003-0029-1541

Arindam Chowdhury − *Department of Chemistry, Indian Institute of Technology Bombay, 400076 Mumbai, India;* orcid.org/0000-0001-8178-1061

Complete contact information is available at: https://pubs.acs.org/10.1021/acsaem.3c00232

Author Contributions

N.S. is responsible for planning and execution of the work and the draft writing. S.K.S. conceived the work and performed the final editing of the manuscript. Other authors helped in the process of experiments and interpretation.

Notes

The authors declare no competing financial interest.

■ ACKNOWLEDGMENTS

The authors thank the Ministry of New and Renewable Energy, Government of India, for the financial support. A.C. thanks the Department of Science and Technology (DST), Government of India, for the financial support. N.S., S.G., S.B., and T.B. thank the Prime Minister Research Fellowship, University Grant Commission (UGC), and Council of Scientific and Industrial Research (CSIR), Government of India, respectively, for predoctoral fellowships. The authors thank Arfin Habibul and Angshuman Nag from the Indian Institute of Science Education and Research, Pune, for their support in optical measurements and the Indus Synchrotron Utilization Division and IIT Bombay ESCA facility for the XPS measurements.

■ REFERENCES

(1) Green, M. A.; Dunlop, E. D.; Hohl-Ebinger, J.; Yoshita, M.; Kopidakis, N.; Hao, X. Solar Cell Efficiency Tables (Version 59). *Prog. Photovoltaics* **2022**, *30*, 3−12.

(2) *NREL Efficiency Chart*, https://www.nrel.gov/pv/cell-efficiency.html (accessed July, 2022).

(3) Kojima, A.; Teshima, K.; Shirai, Y.; Miyasaka, T. Organometal Halide Perovskites as Visible-Light Sensitizers for Photovoltaic Cells. *J. Am. Chem. Soc.* **2009**, *131*, 6050−6051.

(4) Min, H.; Lee, D. Y.; Kim, J.; Kim, G.; Lee, K. S.; Kim, J.; Paik, M. J.; Kim, Y. K.; Kim, K. S.; Kim, M. G.; Shin, T. J.; Il Seok, S. Perovskite Solar Cells with Atomically Coherent Interlayers on SnO_2 Electrodes. *Nature* **2021**, *598*, 444−450.

(5) Saliba, M.; Correa-Baena, J. P.; Wolff, C. M.; Stolterfoht, M.; Phung, N.; Albrecht, S.; Neher, D.; Abate, A. How to Make over 20% Efficient Perovskite Solar Cells in Regular (n-i-p) and Inverted (p-i-n) Architectures. *Chem. Mater.* **2018**, *30*, 4193−4201.

(6) Lee, D.-K.; Park, N. Materials and Methods for High-Efficiency Perovskite Solar Modules. *Sol. RRL* **2022**, *6*, No. 2100455.

(7) Azmi, R.; Ugur, E.; Seitkhan, A.; Aljamaan, F.; Subbiah, A. S.; Liu, J.; Harrison, G. T.; Nugraha, M. I.; Eswaran, M. K.; Babics, M.; Chen, Y.; Xu, F.; Allen, T. G.; Rehman, A.; Wang, C.; Anthopoulos, T. D.; Schwingenschlögl, U.; Bastiani, M.; De; Aydin, E.; Wolf, S. De. Damp Heat − Stable Perovskite Solar Cells with Tailored-Dimensionality 2D/3D Heterojunctions. *Science* **2022**, *376*, 73−77.

(8) Ghosh, S.; Singh, R.; Subbiah, A. S.; Boix, P. P.; Mora Seró, I.; Sarkar, S. K. Enhanced Operational Stability through Interfacial Modification by Active Encapsulation of Perovskite Solar Cells. *Appl. Phys. Lett.* **2020**, *116*, No. 113502.

(9) Martin, B.; Amos, D.; Brehob, E.; van Hest, M. F. A. M.; Druffel, T. Techno-Economic Analysis of Roll-to-Roll Production of Perovskite Modules Using Radiation Thermal Processes. *Appl. Energy* **2022**, *307*, No. 118200.

(10) Yang, Z.; Zhang, W.; Wu, S.; Zhu, H.; Liu, Z.; Liu, Z.; Jiang, Z.; Chen, R.; Zhou, J.; Lu, Q.; Xiao, Z.; Shi, L.; Chen, H.; Ono, L. K.; Zhang, S.; Zhang, Y.; Qi, Y.; Han, L.; Chen, W. Slot-Die Coating Large-Area Formamidinium-Cesium Perovskite Film for Efficient and Stable Parallel. Solar Module. *Sci. Adv.* **2021**, *7*, 1−14.

(11) Liu, K.; Liang, Q.; Qin, M.; Shen, D.; Yin, H.; Ren, Z.; Zhang, Y.; Zhang, H.; Fong, P. W. K.; Wu, Z.; Huang, J.; Hao, J.; Zheng, Z.; So, S. K.; Lee, C. S.; Lu, X.; Li, G. Zwitterionic-Surfactant-Assisted Room-Temperature Coating of Efficient Perovskite Solar Cells. *Joule* **2020**, *4*, 2404−2425.

(12) Tang, S.; Bing, J.; Zheng, J.; Tang, J.; Li, Y.; Mayyas, M.; Cho, Y.; Jones, T. W.; Yang, T. C. J.; Yuan, L.; Tebyetekerwa, M.; Nguyen, H. T.; Nielsen, M. P.; Ekins-Daukes, N. J.; Kalantar-Zadeh, K.; Wilson, G. J.; McKenzie, D. R.; Huang, S.; Ho-Baillie, A. W. Y. Complementary Bulk and Surface Passivations for Highly Efficient Perovskite Solar Cells by Gas Quenching. *Cell Rep. Phys. Sci.* **2021**, *2*, No. 100511.

(13) Uddin, A.; Yi, H. Progress and Challenges of SnO2 Electron Transport Layer for Perovskite Solar Cells: A Critical Review. *Sol. RRL* **2022**, *6*, No. 2100983.

(14) Petrović, M.; Maksudov, T.; Panagiotopoulos, A.; Serpetzoglou, E.; Konidakis, I.; Stylianakis, M. M.; Stratakis, E.; Kymakis, E. Limitations of a Polymer-Based Hole Transporting Layer for Application in Planar Inverted Perovskite Solar Cells. *Nanoscale Adv.* **2019**, *1*, 3107−3118.

(15) Subbiah, A. S.; Isikgor, F. H.; Howells, C. T.; De Bastiani, M.; Liu, J.; Aydin, E.; Furlan, F.; Allen, T. G.; Xu, F.; Zhumagali, S.; Hoogland, S.; Sargent, E. H.; McCulloch, I.; De Wolf, S. High-Performance Perovskite Single-Junction and Textured Perovskite/Silicon Tandem Solar Cells via Slot-Die-Coating. *ACS Energy Lett.* **2020**, *5*, 3034−3040.

(16) Abdollahi Nejand, B.; Nazari, P.; Gharibzadeh, S.; Ahmadi, V.; Moshaii, A. All-Inorganic Large-Area Low-Cost and Durable Flexible Perovskite Solar Cells Using Copper Foil as a Substrate. *Chem. Commun.* **2017**, *53*, 747−750.

(17) Heo, J. H.; Shin, D. H.; Lee, M. L.; Kang, M. G.; Im, S. H. Efficient Organic-Inorganic Hybrid Flexible Perovskite Solar Cells Prepared by Lamination of Polytriarylamine/CH3NH3PbI3/Anodized Ti Metal Substrate and Graphene/PDMS Transparent Electrode Substrate. *ACS Appl. Mater. Interfaces* **2018**, *10*, 31413−31421.

(18) Dai, X.; Deng, Y.; Van Brackle, C. H.; Chen, S.; Rudd, P. N.; Xiao, X.; Lin, Y.; Chen, B.; Huang, J. Scalable Fabrication of Efficient Perovskite Solar Modules on Flexible Glass Substrates. *Adv. Energy Mater.* **2020**, *10*, No. 1903108.

(19) Galagan, Y.; Di Giacomo, F.; Gorter, H.; Kirchner, G.; de Vries, I.; Andriessen, R.; Groen, P. Roll-to-Roll Slot Die Coated Perovskite for Efficient Flexible Solar Cells. *Adv. Energy Mater.* **2018**, *8*, No. 1801935.

(20) Dou, B.; Whitaker, J. B.; Bruening, K.; Moore, D. T.; Wheeler, L. M.; Ryter, J.; Breslin, N. J.; Berry, J. J.; Garner, S. M.; Barnes, F. S.; Shaheen, S. E.; Tassone, C. J.; Zhu, K.; Van Hest, M. F. A. M. Roll-to-Roll Printing of Perovskite Solar Cells. *ACS Energy Lett.* **2018**, *3*, 2558−2565.

(21) Palneedi, H.; Park, J. H.; Maurya, D.; Peddigari, M.; Hwang, G. T.; Annapureddy, V.; Kim, J. W.; Choi, J. J.; Hahn, B. D.; Priya, S.; Lee, K. J.; Ryu, J. Laser Irradiation of Metal Oxide Films and Nanostructures: Applications and Advances. *Adv. Mater.* **2018**, *30*, No. 1705148.

(22) Kim, Y. H.; Heo, J. S.; Kim, T. H.; Park, S.; Yoon, M. H.; Kim, J.; Oh, M. S.; Yi, G. R.; Noh, Y. Y.; Park, S. K. Flexible Metal-Oxide

Devices Made by Room-Temperature Photochemical Activation of Solgel Films. *Nature* **2012**, *489*, 128−132.
(23) Subbiah, A. S.; Mathews, N.; Mhaisalkar, S.; Sarkar, S. K. Novel Plasma-Assisted Low-Temperature-Processed SnO_2 Thin Films for Efficient Flexible Perovskite Photovoltaics. *ACS Energy Lett.* **2018**, *3*, 1482−1491.
(24) Singh, C. C.; Roy Choudhury, A. N.; Sutar, D. S.; Sarkar, S. K. Plasma-Assisted Combustion Synthesis of p -Type Transparent Cu Incorporated NiO Thin Films - Correlation between Deposition Chemistry and Charge Transport Characteristics. *J. Appl. Phys.* **2021**, *129*, No. 095104.
(25) Beshkov, G.; Kolentsov, K.; Yourukova, L.; Rachkova, A.; Mateeva, D. Influence of Rapid Thermal Annealing on the Properties of SnO_2 Thin Films. *Mater. Sci. Eng. B* **1995**, *30*, 1−5.
(26) Xu, W.; Daunis, T. B.; Piper, R. T.; Hsu, J. W. P. Effects of Photonic Curing Processing Conditions on $MAPbI_3$ Film Properties and Solar Cell Performance. *ACS Appl. Energy Mater.* **2020**, *3*, 8636−8645.
(27) Ghahremani, A. H.; Pishgar, S.; Bahadur, J.; Druffel, T. Intense Pulse Light Annealing of Perovskite Photovoltaics Using Gradient Flashes. *ACS Appl. Energy Mater.* **2020**, *3*, 11641−11654.
(28) Sanchez, S.; Christoph, N.; Grobety, B.; Phung, N.; Steiner, U.; Saliba, M.; Abate, A. Efficient and Stable Inorganic Perovskite Solar Cells Manufactured by Pulsed Flash Infrared Annealing. *Adv. Energy Mater.* **2018**, *8*, No. 1802060.
(29) Castriotta, L. A.; Matteocci, F.; Vesce, L.; Cinà, L.; Agresti, A.; Pescetelli, S.; Ronconi, A.; Löffler, M.; Stylianakis, M. M.; Di Giacomo, F.; Mariani, P.; Stefanelli, M.; Speller, E. M.; Alfano, A.; Paci, B.; Generosi, A.; Di Fonzo, F.; Petrozza, A.; Rellinghaus, B.; Kymakis, E.; Di Carlo, A. Air-Processed Infrared-Annealed Printed Methylammonium-Free Perovskite Solar Cells and Modules Incorporating Potassium-Doped Graphene Oxide as an Interlayer. *ACS Appl. Mater. Interfaces* **2021**, *13*, 11741−11754.
(30) Daunis, T. B.; Schroder, K. A.; Hsu, J. W. P. Photonic Curing of Solution-Deposited ZrO_2 Dielectric on PEN: A Path towards High-Throughput Processing of Oxide Electronics. *npj Flexible Electron.* **2020**, *4*, No. 7.
(31) Troughton, J.; Carnie, M. J.; Davies, M. L.; Charbonneau, C.; Jewell, E. H.; Worsley, D. A.; Watson, T. M. Photonic Flash-Annealing of Lead Halide Perovskite Solar Cells in 1 ms. *J. Mater. Chem. A* **2016**, *4*, 3471−3476.
(32) Das, S.; Gu, G.; Joshi, P. C.; Yang, B.; Aytug, T.; Rouleau, C. M.; Geohegan, D. B.; Xiao, K. Low Thermal Budget, Photonic-Cured Compact TiO_2 Layers for High-Efficiency Perovskite Solar Cells. *J. Mater. Chem. A* **2016**, *4*, 9685−9690.
(33) Feleki, B.; Bex, G.; Andriessen, R.; Galagan, Y.; Di Giacomo, F. Rapid and Low Temperature Processing of Mesoporous TiO_2 for Perovskite Solar Cells on Flexible and Rigid Substrates. *Mater. Today Commun.* **2017**, *13*, 232−240.
(34) Zhu, M.; Liu, W.; Ke, W.; Clark, S.; Secor, E. B.; Song, T. B.; Kanatzidis, M. G.; Li, X.; Hersam, M. C. Millisecond-Pulsed Photonically-Annealed Tin Oxide Electron Transport Layers for Efficient Perovskite Solar Cells. *J. Mater. Chem. A* **2017**, *5*, 24110−24115.
(35) Ghahremani, A. H.; Martin, B.; Gupta, A.; Bahadur, J.; Ankireddy, K.; Druffel, T. Rapid Fabrication of Perovskite Solar Cells through Intense Pulse Light Annealing of SnO_2 and Triple Cation Perovskite Thin Films. *Mater. Des.* **2020**, *185*, No. 108237.
(36) Oh, K.; Jung, K.; Shin, J.; Ko, S.; Lee, M. J. Novel Intense-Pulsed-Light Synthesis of Amorphous SnO_2 Electron-Selective Layers for Efficient Planar $MAPbI_3$ Perovskite Solar Cells. *J. Mater. Sci. Technol.* **2021**, *92*, 171−177.
(37) Li, Z.; Wang, L.; Liu, R.; Fan, Y.; Meng, H.; Shao, Z.; Cui, G.; Pang, S. Spontaneous Interface Ion Exchange: Passivating Surface Defects of Perovskite Solar Cells with Enhanced Photovoltage. *Adv. Energy Mater.* **2019**, *9*, No. 1902142.
(38) Jang, Y.; Lee, H.; Char, K. Transparent Thin Film Transistors of Polycrystalline SnO_{2-x} and Epitaxial SnO_{2-X}. *AIP Adv.* **2020**, *10*, No. 035011.
(39) Zhu, P.; Gu, S.; Luo, X.; Gao, Y.; Li, S.; Zhu, J.; Tan, H. Simultaneous Contact and Grain-Boundary Passivation in Planar Perovskite Solar Cells Using SnO_2-KCl Composite Electron Transport Layer. *Adv. Energy Mater.* **2020**, *10*, No. 1903083.
(40) Rau, U. Reciprocity Relation between Photovoltaic Quantum Efficiency and Electroluminescent Emission of Solar Cells. *Phys. Rev. B - Condens. Matter Mater. Phys.* **2007**, *76*, No. 085303.
(41) Nayak, P. K.; Mahesh, S.; Snaith, H. J.; Cahen, D. Photovoltaic Solar Cell Technologies: Analysing the State of the Art. *Nat. Rev. Mater.* **2019**, *4*, 269−285.
(42) Bertoluzzi, L.; Sanchez, R. S.; Liu, L.; Lee, J. W.; Mas-Marza, E.; Han, H.; Park, N. G.; Mora-Sero, I.; Bisquert, J. Cooperative Kinetics of Depolarization in $CH_3NH_3PbI_3$ Perovskite Solar Cells. *Energy Environ. Sci.* **2015**, *8*, 910−915.
(43) Hu, J.; Gottesman, R.; Gouda, L.; Kama, A.; Priel, M.; Tirosh, S.; Bisquert, J.; Zaban, A. Photovoltage Behavior in Perovskite Solar Cells under Light-Soaking Showing Photoinduced Interfacial Changes. *ACS Energy Lett.* **2017**, *2*, 950−956.
(44) Gottesman, R.; Lopez-Varo, P.; Gouda, L.; Jimenez-Tejada, J. A.; Hu, J.; Tirosh, S.; Zaban, A.; Bisquert, J. Dynamic Phenomena at Perovskite/Electron-Selective Contact Interface as Interpreted from Photovoltage Decays. *Chem* **2016**, *1*, 776−789.
(45) Wu, J.; Shi, J.; Li, Y.; Li, H.; Wu, H.; Luo, Y.; Li, D.; Meng, Q. Quantifying the Interface Defect for the Stability Origin of Perovskite Solar Cells. *Adv. Energy Mater.* **2019**, *9*, No. 1901352.

https://doi.org/10.1021/acsaem.3c00232
ACS Appl. Energy Mater. XXXX, XXX, XXX−XXX